



Contents lists available at ScienceDirect

# Sensors and Actuators B: Chemical

journal homepage: [www.elsevier.com/locate/snb](http://www.elsevier.com/locate/snb)



## A microfluidic platform with integrated flow sensing for focal chemical stimulation of cells and tissue

Jonathan T.W. Kuo<sup>a</sup>, Li-Yuan Chang<sup>a</sup>, Po-Ying Li<sup>b</sup>, Tuan Hoang<sup>a</sup>, Ellis Meng<sup>a,b,\*</sup>

<sup>a</sup> Biomedical Microsystems Laboratory, Department of Biomedical Engineering, University of Southern California, Los Angeles, CA, United States

<sup>b</sup> Ming Hsieh Department of Electrical Engineering, University of Southern California, Los Angeles, CA, United States

### ARTICLE INFO

#### Article history:

Received 8 July 2010

Received in revised form

10 December 2010

Accepted 14 December 2010

Available online 21 December 2010

#### Keywords:

Parylene C

Focal chemical stimulation

Neural interface

Chemical interface

Fluid delivery

### ABSTRACT

A microfluidic platform for precise biochemical control of the extracellular microenvironment was developed. A chemical interface was established with cells or tissues through the precise and focal delivery of soluble chemical agents through a pore addressed by a polymer microchannel. Thermal flow sensors were integrated along the length of the microchannel and monitored internal flow rate. Sensor performance was characterized in anticipation of future studies with real-time feedback control of focal delivery. The microfluidic system was characterized by determining the fluid delivery rates through the pores and concentration profiles of agents delivered. Finally, focal delivery to rat retinal tissue was demonstrated.

© 2010 Elsevier B.V. All rights reserved.

### 1. Introduction

The cellular microenvironment contains a number of chemical gradients that fundamentally influence cell functions such as cell signaling, nutrient uptake, waste disposal, and gas exchange. Thus, control of these microenvironments is sought to enable precise studies of cells and tissues both in vitro and in vivo. The conventional method to control microenvironments is by releasing soluble factors to cells through bulk fluid flow delivered by hand-pipetting or other forms of perfusion and targets only large cell populations. However, this crude method does not allow for precise modulation of the cellular microenvironment for a targeted cell or small cell group within a population [1,2]. A focused chemical stimulus in the targeted microenvironment of a cell within a population can evoke a specific response that elucidates its relationship within the cellular network or tissue organization.

Devices that allow precise and repeatable modulation of the cellular microenvironment would benefit biological applications in which precise control over the microenvironment is required such as stem cell niches, selective differentiation, metaplasia (reversible transformation of cell from normal to abnormal state), synap-

togenesis, and chemotaxis [1,3–8]. Microfluidic dosing devices that enable selective stimulation of cells have been introduced [1,2,9–12]. Devices that produce controlled laminar flows defined by microchannels have demonstrated cellular and sub-cellular resolution of cell inactivation by changing the localized microenvironment of cells cultured in the microchannels [2,10,11]. For example, Tourovskaia et al. demonstrated localized stimulation of muscle cells cultured within a main poly(dimethylsiloxane) channel 2 cm long, 1500  $\mu\text{m}$  wide, and 250  $\mu\text{m}$  high with a hydrodynamically focused agrin stream ( $\sim 100$ – $150$   $\mu\text{m}$  wide) delivered by a central inlet channel connected to the main channel [2]. However, these devices are suitable for cell culture studies but are difficult to use with tissue samples.

Another method of controlling the microenvironment is to release soluble factors from a small aperture (2–8  $\mu\text{m}$  in diameter) [1,2,9]. This technique can produce repeatable localized chemical gradients at multiple locations on a device and is applicable for tissue applications. Agrin was focally applied via a microaperture array to myotubes cultured on top of the array; apertures (ranging 2–8  $\mu\text{m}$  diameter) were etched into a low-stress silicon nitride membrane and useful in studies of neuromuscular synaptogenesis [1]. Technology for the localized delivery of soluble agents is also beneficial not only for the study of in vitro or ex vivo systems but also for in vivo therapeutic applications such as drug delivery and neurotransmitter-based biomimetic neural prostheses [1,2,9,12–14]. A neural prostheses intended for restoring vision was devised in which a flow control channel and aperture were used to control neurotransmitter release from each aperture and

\* Corresponding author at: Department of Biomedical Engineering, University of Southern California, 1042 Downey Way, DRB-140, Los Angeles, CA 90089-1111, United States. Tel.: +1 213 740 6952; fax: +1 213 821 3897.

E-mail address: [ellis.meng@usc.edu](mailto:ellis.meng@usc.edu) (E. Meng).

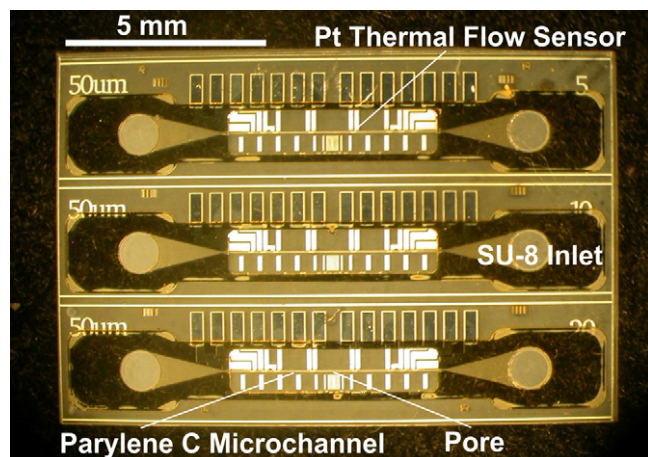


**Fig. 1.** Top view of a microfluidic platform with three 50  $\mu\text{m}$  wide Parylene microchannels. Each channel is centrally perforated with a pore having a size indicated by the label on the upper right corner of each channel (5, 10, 20  $\mu\text{m}$  diameter). Eight Pt thermal flow sensors line each channel and flank the central pore.

thus achieve localized neurotransmitter stimulation of neurons in the visual pathway [12].

Despite the advances summarized above, no microfluidic focal delivery devices currently include integrated flow rate monitoring for accurate determination of flow rate or volume delivered. Thus, a novel microfluidic platform was developed that is capable of controlled fluid delivery from a “pore” to a cellular microenvironment with both passive (diffusion) and active (ejection) modes. Each pore is addressed by its own dedicated microchannel. This microfluidic delivery platform is the first to integrate thermal flow sensors for monitoring the flow rate of each microchannel and so feedback control of focal delivery for each pore is achievable. Arrays of thermal flow sensors made of resistive elements have proven to be simple to fabricate in MEMS processing, useful in many modes of operation (hot-film, calorimetric, and time-of-flight), and can be used to determine the thermal properties of the working fluid [15–18]. The thermal flow sensors in the microfluidic platform are capable of detecting flow rates of nL/min. Fluid delivery from different sized pores was investigated and preliminary focal delivery to tissue was demonstrated.

## 2. Design

The microfluidic platform consists of an array of three surface micromachined Parylene C microchannels on a soda lime glass substrate (Fig. 1). The microchannels measure 6 mm  $\times$  100  $\mu\text{m}$   $\times$  4  $\mu\text{m}$  ( $L \times W \times H$ ) with 2  $\mu\text{m}$  thick walls. Each microchannel is perforated by a centrally located pore that is flanked by a linear array of platinum thermal flow sensors (Fig. 2). Pore sizes of 5, 10 or 20  $\mu\text{m}$  in

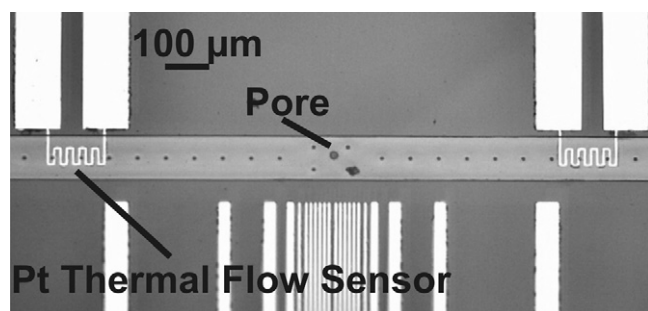


**Fig. 2.** Close up view of one of the Parylene microchannels (100  $\mu\text{m}$  wide). The Pt thermal flow sensors and pore (20  $\mu\text{m}$  diameter) can be clearly seen.

diameter were used. SU-8 structures provide inlet and outlet access ports (1 mm in diameter) for macro-world fluidic access from the top of the chip and eliminate the need for through-wafer etching. A funnel structure connects the access ports to the microchannel and its top wall is supported by Parylene posts for increased mechanical robustness to prevent collapse of the wide, free-standing structure.

Parylene C was chosen as the structural material of the microchannels for its proven bioinert property as well as in vitro cytocompatibility [17,19–23]. Since the microchannels will be placed in direct contact with cells/tissue, biocompatibility is a priority for stable long-term studies. Parylene C is also compatible with low temperature microfabrication processes, including those required to easily form surface micromachined channels [24–26]. The transparency of Parylene C and the supporting glass substrate allow for real-time visual inspection of flow within the microchannel, localized ejection of chemicals at the pore, and the biological response of the cells/tissue to the focal chemical gradient using optical microscopy techniques.

Platinum thermal flow sensors made of thin film resistors were chosen for their ease of fabrication and proven flow sensing properties: high corrosion and oxidation resistance, large temperature range, linear resistance versus temperature relationship, and high temperature coefficient of resistivity (TCR) [17,27–32]. A Parylene C insulation layer over the thermal flow sensors prevents undesirable reactions with conductive solutions.

## 3. Theory

### 3.1. Thermal flow sensing

Thermal flow measurement relies on convective heat loss from a heated resistive element into the surrounding fluid flow. The resistive element or flow sensor is electrically heated above the fluid temperature and experiences a loss of heat proportional to the fluid thermal conductivity and experienced flow velocity. Six different operational modes are possible with thermal flow measurement by controlling either the heating power or temperature and monitoring the heater temperature, power, or temperature difference [33]. Hot-film mode was investigated for this study for its ease of implementation.

Sensors are located adjacent to the fluid flow and experience convective heat loss that increases with fluid velocity in hot-film mode. Monitoring the resistance or voltage change of the sensor yields an indirect measure of flow rate that is first calibrated against a known imposed flow rate. For typical thermal flow sensor materials, the resistance relationship to temperature is given by:

$$R(T) = R(T_0)[1 + \alpha(T - T_0)] \quad (1)$$

where  $R(T)$  is the resistance at temperature  $T$  and  $\alpha$  is the TCR. TCR can be determined experimentally by:

$$a_R = \frac{R(T) - R(T_0)}{R(T_0)} = \alpha(T - T_0) \quad \text{or} \quad \frac{\Delta R}{R} = \alpha \Delta T \quad (2)$$

in which  $a_R$  is the resistance overheat ratio and determined by measuring the change in resistance of the material at two different temperatures. Hot-film sensors can be operated in constant current or constant temperature modes [34]. In constant current (CC) mode, the current bias imposed on the sensor is held constant and the flow rate is measured by monitoring the change in resistance (or voltage) due to the resulting temperature change of the sensor. In constant temperature (CT) mode, feedback circuitry is used to hold the temperature of the sensor constant and the increase in heating power needed to maintain that temperature in response to convective heat loss to the adjacent fluid flow is measured. CT mode, although more difficult to implement, can offer better resolution and frequency response over CC mode [18].

### 3.2. Diffusion modeling

Diffusion of fluid from the pore in the microchannel can be modeled with a constant point source diffusion concentration profile given by:

$$\begin{aligned} u(t, x) &= C_1 [1 - \operatorname{erf}(x/\sqrt{4Dt})] \\ \frac{\partial u}{\partial t} &= D \frac{\partial^2 u}{\partial x^2}, \quad t > 0, x \in (0, \infty), \\ u(t, 0) &= C_1, \lim_{x \rightarrow \infty} u(t, x) = 0, \\ u(0, x) &= 0, \quad x \in (0, \infty) \end{aligned} \quad (3)$$

where  $u$  is concentration,  $D$  is the diffusion coefficient,  $x$  is the distance from the aperture,  $t$  is time, and  $C_1$  is the initial concentration.

### 4. Fabrication

Devices were fabricated on piranha ( $\text{H}_2\text{SO}_4:\text{H}_2\text{O}_2$  4:1) cleaned 3" soda lime substrates (Fig. 3). First, Pt thermal sensors were defined using a standard liftoff process. AZ4400 (AZ Electronic Materials, Branchburg, NJ) photoresist was applied (3 krpm, 30 s), softbaked (90 °C for 3 min), and exposed. Following development in AZ351 (diluted 1:4 with deionized  $\text{H}_2\text{O}$ , AZ Electronic Materials, Branchburg, NJ), a short descum step was performed ( $\text{O}_2$  plasma: 100 mTorr, 60 W, and 1 min). Ti/Pt (200 Å/2000 Å) were deposited by electron-beam evaporation and subsequently defined by liftoff in sequential immersions with gentle mechanical agitation in acetone, isopropyl alcohol, and deionized water. Following a short descum to clean the surface ( $\text{O}_2$  plasma: 100 mTorr, 60 W, and 1 min), adhesion promoter (A-174, Specialty Coating Systems, Indianapolis, IN) was applied following the manufacturer's standard recipe and a Parylene C film (2 µm) was vapor deposited (Labcoater 2010, Specialty Coating Systems, Indianapolis).

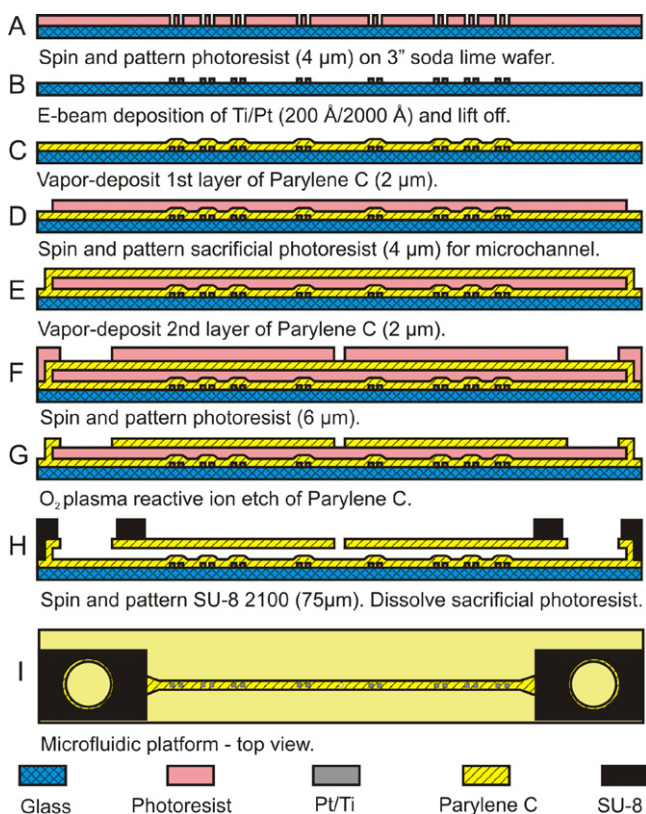


Fig. 3. Fabrication process for creating the microfluidic platform.

Next, microchannels were fabricated using surface micromachining techniques. Sacrificial photoresist (4 µm AZ4400) was spun on (3 krpm, 30 s), exposed, and developed (diluted AZ351) to define both the channel pattern and small pits that eventually form support posts along the channel length to prevent collapse. A short descum was performed to clean the surface ( $\text{O}_2$  plasma: 100 mTorr, 60 W, and 1 min) and then channels were completed by depositing a second layer of Parylene C (4 µm). This Parylene layer was etched to obtain fluidic access to the channel, form the central fluid delivery pore, and create contact pad openings to the thermal sensor elements. AZ4400 (6 µm) was applied (2 krpm, 30 s), exposed, and developed (diluted AZ351). Parylene was etched in oxygen plasma in a reactive ion etcher (200 mTorr and 150 W) [20]. Any remaining photoresist was removed and the surface was descumed ( $\text{O}_2$  plasma: 100 mTorr, 50 W and 30 s).

Finally, the SU-8 fluidic ports were fabricated at the inlet and outlet to facilitate fluidic access to the Parylene channels and prevent mechanical damage to the structure during packaging [35]. SU-8 2100 (Microchem Corp., Newton, MA) was spun on (2 krpm, 30 s, 75 µm), softbaked (7 min at 65 °C and 30 min at 90 °C both with a 3 °C/min ramp), exposed (360 mJ/cm<sup>2</sup>), post exposure baked (5 min at 65 °C then 8 min at 95 °C both with a 3 °C/min ramp), developed, and hardbaked (30 min at 100 °C with a 3 °C/min ramp). Individual dies were diced and separated. To remove the sacrificial photoresist in the channels, dies were immersed in isopropyl alcohol (IPA) over several days then rinsed clean in deionized water before use. IPA was used instead of acetone to remove the sacrificial photoresist. Although the dissolution process is significantly slower, this eliminates SU-8 cracking or delamination from the inlet/outlet ports due to large stresses resulting from exposure to acetone.

### 5. Packaging

A custom made acrylic jig was fabricated using a laser drill (Mini/Helix 8000, Epilog, Golden, CO) to package the microfluidic platform to allow for simultaneous fluidic and electrical connections (Fig. 4). Sylgard 184 (Dow Corning, Midland, MI) was used to make gaskets to create a seal around the inlet and outlet ports of the microchannel. Glass capillaries (5 µL, Alltech, Deerfield, IL) were inserted through the top of the jig into the PDMS gaskets to create fluidic connections into and out of the channel.

The microfluidic platform was first bonded to a custom PCB using standard epoxy. The electrical contact pads on the microflu-

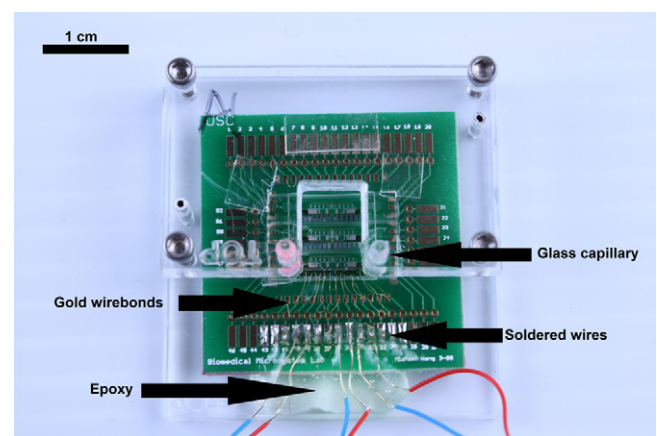


Fig. 4. Packaged microfluidic platform in a custom made acrylic jig with gold wirebonds connecting the embedded Pt thermal flow sensors to the PCB. Wires were soldered to the PCB and covered with epoxy to make robust external electrical connections. Glass capillaries aligned to and clamped on top of the SU-8 inlet/outlets provided a fluidic connection to the microchannel.



idic platform were then wire bonded (Au) to the PCB. Finally, wires were soldered to the PCB for external electrical connections to the embedded flow sensors.

The microfluidic platform bonded to the PCB was then carefully aligned between the top and bottom pieces of the acrylic jig to make sure the position of the glass capillaries matched the inlet and outlet ports of the device. The two pieces of the jig were then tightened together by screws, securing the device.

PEEK tubing was used to connect to the glass capillaries with a short piece of silicone tubing acting as a transition tube. The other end of the PEEK tubing was connected to a precision glass syringe (Gastight Syringes, Hamilton Company, Reno, NV) driven by a syringe pump (PHD 2000, Harvard Apparatus Inc., Holliston, MA).

## 6. Experimental methods

### 6.1. Benchtop calibration of flow sensors

First, the zero power resistance of each flow sensor was determined by linear extrapolation from resistances measured at two different applied currents (2400 SourceMeter, Keithley Instruments Inc., Cleveland, OH). Next, the linear current–voltage relationship of the flow sensors was verified. The temperature coefficient of resistance of a flow sensor was calculated from device resistance measurements (2700 MultiMeter, Keithley Instruments Inc., Cleveland, OH) obtained at known temperatures applied by a programmable oven (Environmental Chamber, Sun Electronic Systems Inc., Titusville, FL). This process was controlled and automated with a custom LabVIEW program. The ratio of the change in resistance to nominal resistance, or resistance overheat ratio ( $a_R$ ), was calculated and used to determine the temperature rise of the resistive sensor, or overheat temperature (OHT), from the applied current.

### 6.2. Flow sensor calibration in hot-film mode

The hot-film method tracks fluid flow by measuring convective heat loss from the heated flow sensor to the fluid. Two different hot-film modes (constant current and constant temperature) were investigated with devices that had the pore plugged by a drop of epoxy as shown in Fig. 5. The packaged device was placed in an oven for thermal isolation to minimize interference from fluctuations

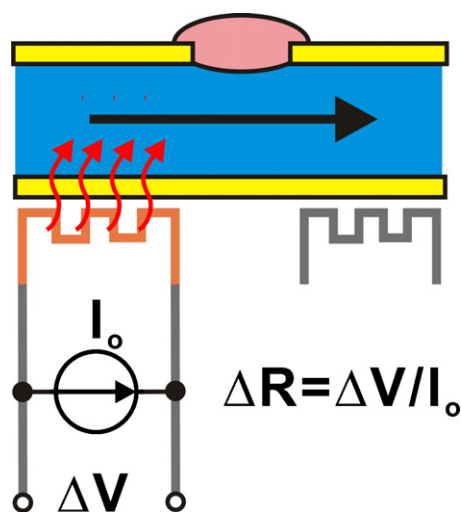


**Fig. 5.** Illustration of thermal flow sensing principle under constant current hot-film mode. The pore is plugged and forced convection of heat by fluid flow is detected by the change in voltage in the resistive sensing element.

in the ambient temperature. A small opening in the oven allowed for fluidic and electric access to the device. Deionized (DI) water was chosen to demonstrate relevant sensor performance since the thermal conductivity of chemical solutions to be delivered in our application are close to that of water.

#### 6.2.1. Constant current

Sensor calibration was performed at three different overheat ratios corresponding to overheat temperatures of 7.4 °C, 10.1 °C, and 13.3 °C. A single flow sensor was connected in a Wheatstone bridge under quarter-bridge configuration. The 2400 SourceMeter provided a constant current source and the 2700 MultiMeter recorded the voltage output of the bridge under the control of a custom LabVIEW program. Filtered DI water was pumped through the microchannel at predetermined flow rates using a syringe pump. Data for each flow rate was acquired after sensor response stabilized and then averaged ( $n = 83$ , 0.5 samples per second).

#### 6.2.2. Constant temperature

Sensor calibration under constant temperature operation was performed at three different overheat ratios (the same ones used in constant current mode). Constant overheat temperature was maintained by using a feedback circuit as previously described [17]. Briefly, the output of a Wheatstone bridge containing the sensor was fed into a negative feedback operational amplifier circuit. Imbalance in the Wheatstone bridge due to cooling of the flow sensor was automatically corrected by the circuit with increased current in order to compensate for resistance and thus temperature change. The output voltage was further amplified to facilitate the measurement. Data was acquired using a custom LabVIEW program interfaced to the 2700 MultiMeter while a syringe pump controlled the flow rate in the microchannels. The output voltage for each flow rate setting was recorded and averaged ( $n = 60$ ).

### 6.3. Thermal flow sensing of fluid delivery through pore

A microchannel was investigated for electrical sensing of fluid delivery through a pore with a diameter of 20 μm. Two flow sensors, one before the pore and one after, were biased at 4 mA in hot-film constant current mode using two separate 2400 SourceMeters as a CC source for each (sensors equidistant from pore, distance between sensors = 4.5 mm). Both sensors were placed in two separate and identical Wheatstone quarter-bridges (Fig. 6). The bridge outputs were simultaneously recorded ( $n = 58$ ) for each flow rate setting (filtered DI water) using two separate channels of the LabView controlled 2700 MultiMeter (Keithley Instruments Inc., Cleveland, OH). The data recorded at each flow rate were then averaged, and the resulting curves were compared to one another.

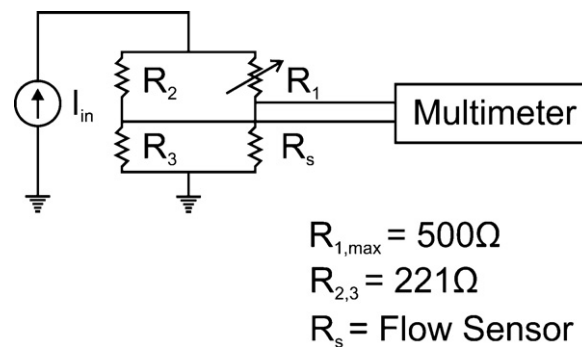


**Fig. 6.** Wheatstone quarter-bridge schematic used for thermal flow sensing of fluid through pore. Two separate and identical bridges were used: one for the sensor before the pore and one after.

#### 6.4. Optical monitoring of fluid delivery through pore

##### 6.4.1. Fluid delivery rate in air

Fluid delivery rates generated through a  $10\ \mu\text{m}$  pore was investigated. Rhodamine B ( $0.11\ \text{mM}$ ) was used as a dye indicator and flowed through the device. This setup was placed underneath a microscope (Motic, Xiamen, China) in order to image the dye bolus ejected from the pore. Different flow rates were applied to the microchannel via syringe pump ( $50\text{--}750\ \text{nL/min}$ ). The dye bolus was estimated to be a hemisphere; the radius was analyzed using NIH ImageJ v1.34 to calculate the delivered volume and hence the flow rate out of the pore. The evaporation rate was measured and the data were corrected to account for evaporative fluid loss over the course of the experiments.

##### 6.4.2. Fluid delivery rate in aqueous solution

Fluid delivery rate into aqueous solution was performed in two modes: diffusion and active ejection. The microchannel was first primed with Rhodamine B. Next, filtered DI water was added to the SU-8 reservoir immersing the pore ( $10\ \mu\text{m}$  diameter). Fluid delivery of Rhodamine B by diffusion through the pore into the water was time-lapse imaged by a fluorescent microscope (Nikon Eclipse LV100, Tokyo, Japan). The optical intensity of the dye was analyzed using NIH ImageJ and normalized for different distances from the aperture or pore. This data was then compared to the predicted results from point source diffusion theory with an initial concentration  $C_1$  set to 1 and the diffusion coefficient  $D$  set to  $2.8 \times 10^{-6}\ \text{cm}^2/\text{s}$  [36].

Fluid delivery of Rhodamine B by active ejection through the pore into the water was conducted for the three different pore sizes at three different input flow rates to the microchannel ( $50, 100, 200\ \text{nL/min}$ ) imposed by a syringe pump. A separate set of experiments were also performed in which a glass coverslip was placed on top of the final SU-8 layer applied to the device ( $75\ \mu\text{m}$  above the pore). In the former case, volume and thus flow rate were estimated by assuming a hemispherical Rhodamine B plume, and for the latter, the volume was assumed to be approximately cylindrical (limited to  $75\ \mu\text{m}$  in height by the glass coverslip).

#### 6.5. Tissue study with diffusion and ejection

In vitro focal delivery from the pore to dissected wildtype Sprague–Dawley rat retinal tissue was performed. The retinal tissue was placed over the microfluidic device and gently held flat against the pore using a ring of Whatman filter paper in combination with a metallic ring clamp (Fig. 7). Rhodamine B was delivered to the tissue through the pore ( $20\ \mu\text{m}$ ). Time-lapsed photography ( $0.25\ \text{s}$  intervals) under a fluorescence microscope was used to record diffusion and ejection of Rhodamine B from the pore into the tissue. Diffusion-based delivery was first performed over a period of  $25\ \text{s}$ . Ejection mode (dye from the pore ejects directly into air as opposed to water) was then initiated by priming the device for  $1\ \text{minute}$  and then delivery was recorded over a  $25\ \text{s}$  period on the same tissue. The images were then processed using NIH ImageJ by subtracting the image at the start when no focal delivery had taken place from subsequent images in order to show the difference due to focal delivery of dye. The tissue was then removed for visual inspection.

## 7. Results and discussion

### 7.1. Benchtop calibration of flow sensors

A representative TCR curve is displayed in Fig. 8. This sensor exhibits a TCR of  $1.9 \times 10^{-3}/^\circ\text{C}$ , which is much less than that of

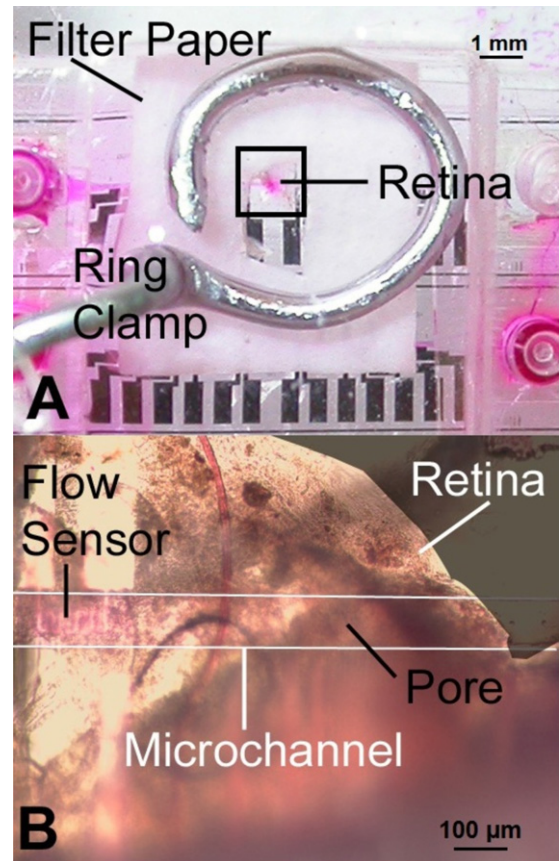


**Fig. 7.** (a) Experimental test setup for Rhodamine B focal delivery to rat retina and (b) zoomed in brightfield image of retinal tissue mounted over a microchannel and pore. Reprinted from Chang, L.Y. et al., Integrated Flow Sensing for Focal Biochemical Stimulation, NEMS 2008, © 2008 IEEE.

bulk Pt but consistent with that of e-beam evaporated Pt thin films [30]. The zero power resistance, IV curve and OHT relationships for a representative sensor are shown in Figs. 9–11, respectively.

The OHT relationship was used to determine the maximum bias current ( $4\ \text{mA}$ ) to keep the flow sensor's overheat temperature below  $15^\circ\text{C}$ . This is to ensure biocompatibility for application with

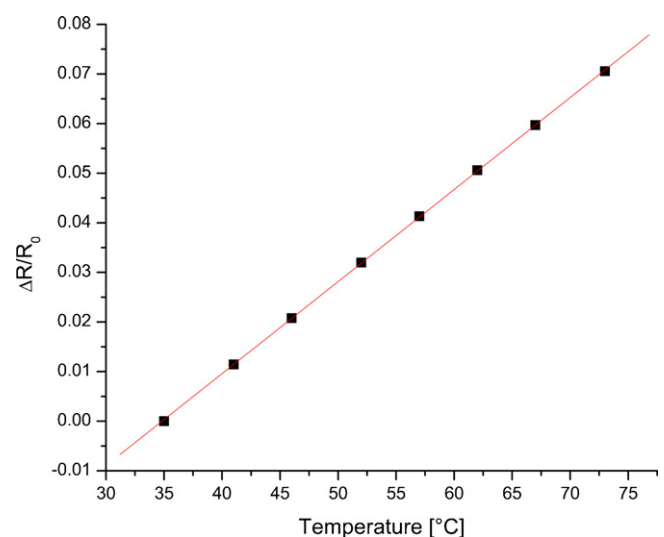


**Fig. 8.** Typical Pt flow sensor TCR curve. This sensor exhibits a TCR of  $1.9 \times 10^{-3}/^\circ\text{C}$ .

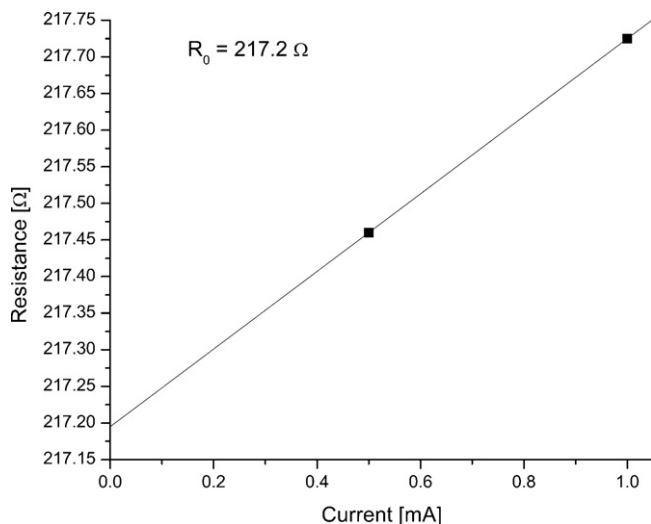


**Fig. 9.** Representative Pt thermal flow sensor zero power resistance result. For this sensor, the zero power resistance is 217.2  $\Omega$ .

cells and tissues and avoid denaturing soluble factors that might be delivered by the microchannel.

## 7.2. Flow sensor calibration in hot-film mode

### 7.2.1. Constant current

A device with the pore sealed was used to calibrate the flow sensors under different applied flow rates at three distinct overheat ratios in constant current injection mode. The resulting voltage change in response to flow rates ranging from 0–1  $\mu\text{L}/\text{min}$  were recorded and averaged (Fig. 12). Kruskal–Wallis non-parametric statistical analysis was performed on the sensor responses and a statistically significant difference ( $p < 0.001$ ) was found between the data taken at different flow rates. At equilibrium, measured responses were stable and thus small changes in flow rate were detectable and discernable despite the low voltage output. Altogether, this suggests a sensor resolution of at least 250 nL/min; lower flow rates were not tested here. Two sensitivity regimes were observed in the flow rate range likely due to thermal time constants associated with the packaging materials. As expected, the CC results

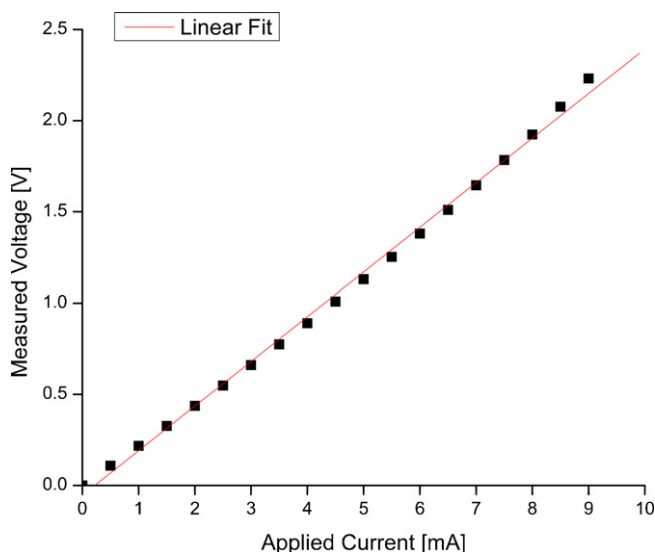


**Fig. 10.** Representative IV curve for a typical sensor. A linear fit was applied to the data (dots).

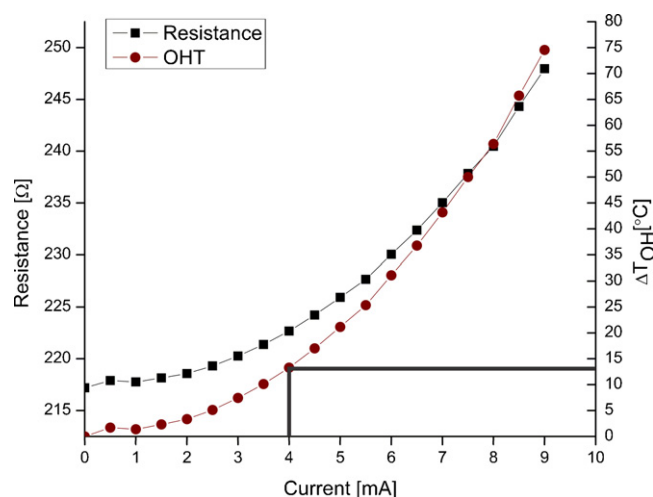


**Fig. 11.** Pt thermal flow sensor overheat behavior. The sensor resistance as a function of applied current was obtained and the overheat temperature was calculated from the empirically determined TCR for the sensor element. In this case, a maximum biasing current of 4 mA corresponding to  $\sim 15^\circ\text{C}$  increase in sensor temperature was applied to all experiments to maintain biocompatibility.

showed greater response to flow rates with higher constant current injection.

### 7.2.2. Constant temperature

The flow sensors were calibrated under CT mode again with controlled flow rates from 0–1  $\mu\text{L}/\text{min}$  at different overheat ratios (Fig. 13). CT mode provided improved flow measurement resolution and greater signal amplitude due to amplification of the voltage output from the feedback circuit. Once again, higher currents corresponding to higher overheat ratios exhibited greater response to changes in flow rate. Despite the increase in complexity of the read-out circuitry, constant temperature mode is further preferred for its increased frequency response over constant current operation [18].

## 7.3. Thermal flow sensing of fluid delivery through pore

A device with an unobstructed pore was used to measure the flow delivered through the pore (DI water) by monitoring the out-

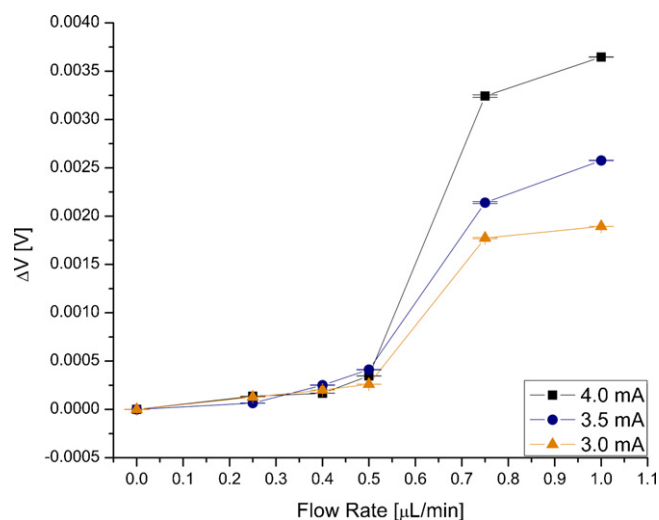


**Fig. 12.** Hot-film responses for three different overheat ratios in constant current biasing (mean  $\pm$  S.E. with  $n = 83$ ). Statistical analysis of the data indicates a significant change in sensor response between all flow rate measurements, so the sensor resolution is at least 250 nL/min.

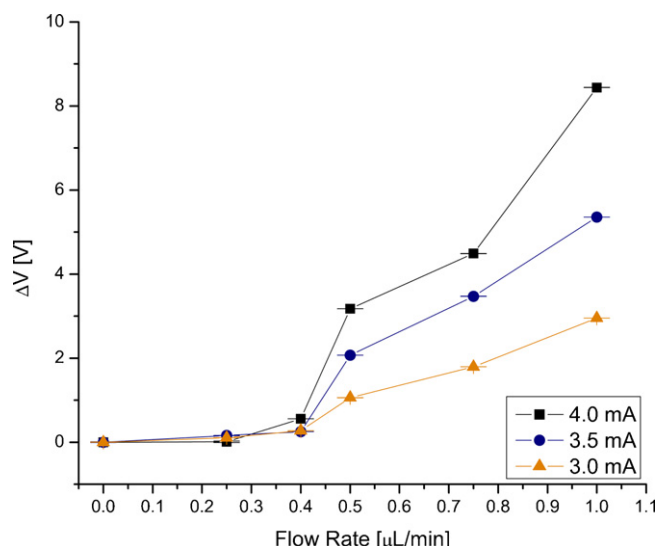


**Fig. 13.** Hot film responses acquired at three different overheat ratios in constant temperature biasing mode (mean  $\pm$  S.E. with  $n = 60$ ) with amplification of output signal by the feedback circuit.

put of two flow sensors, one located upstream of and the other downstream of the pore. Again, known flow rates from 0–1  $\mu\text{L}/\text{min}$  were used and the responses of two sensors were measured and recorded in CC mode (Fig. 14). Fluid delivery through the pore was confirmed by optical inspection under a microscope. For higher flow rates, the upstream sensor exhibited a greater voltage output than the downstream sensor indicating that fluid delivery through the pore can be measured by using this differential measurement technique. However, increased resolution is required for nL/min flows and may be achieved by incorporating thermal isolation structures underneath the sensor regions to prevent undesirable heat transfer to the glass substrate. Statistical analysis (Kruskal–Wallis non-parametric test) was performed on the data and statistically significant differences ( $p < 0.01$ ) were found for all but three points (400 and 1000 nL/min upstream of the pore and 400 nL/min downstream of the pore). One contributing factor is likely the low signal-to-noise ratio.

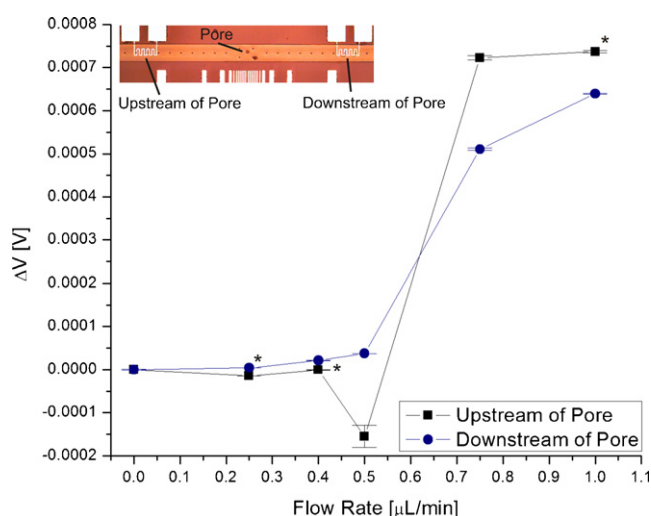


**Fig. 14.** Hot film response for 4 mA constant current biasing for two flow sensors, one upstream and one downstream of the pore in the channel (mean  $\pm$  S.E. with  $n = 58$ ). Both sensors were monitored simultaneously. Data points marked with an asterisk have non-significant changes due to change in flow rate based on statistical analysis. This is attributed to low signal-to-noise ratio.

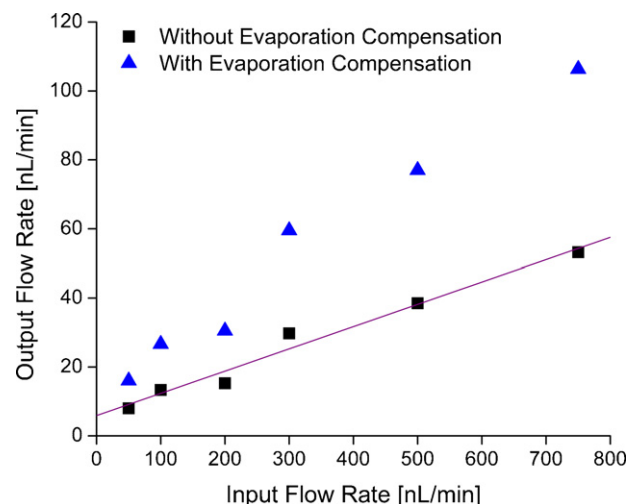


**Fig. 15.** Fluid delivery into air with and without evaporation compensation from a 10  $\mu\text{m}$  pore. A linear fit was applied to the uncompensated data. Reprinted from Chang, L.Y. et al., Integrated Flow Sensing for Focal Biochemical Stimulation, NEMS 2008, © 2008 IEEE.

#### 7.4. Optical monitoring of fluid delivery through pore

##### 7.4.1. Fluid delivery rate in air

The flow rate of fluid ejected from the pore was investigated by flowing dye through the microchannel with different set flow rates from 50 to 750 nL/min. The raw data and corrected data to account for evaporative loss are shown in Fig. 15. As expected, the rate of fluid delivered from the pore has a positive correlation with the flow rate in the microchannel. Fluid delivered from the 10  $\mu\text{m}$  pore ranged from 16 to 106 nL/min. As applied flow rate increased, the proportion of the overall flow delivered through the pore decreased although the fluid delivery rate through the pore increased. The data suggest that localized delivery of pL/nL volumes immediately adjacent to the pore is possible using such an approach.

##### 7.4.2. Fluid delivery rate in aqueous solution

Diffusion from a 10  $\mu\text{m}$  sized pore was investigated and compared to theoretical diffusion in a constant point source model (Fig. 16). The measured diffusion optical intensity profiles (one-dimension) correlate well to those predicted by the model. Thus,

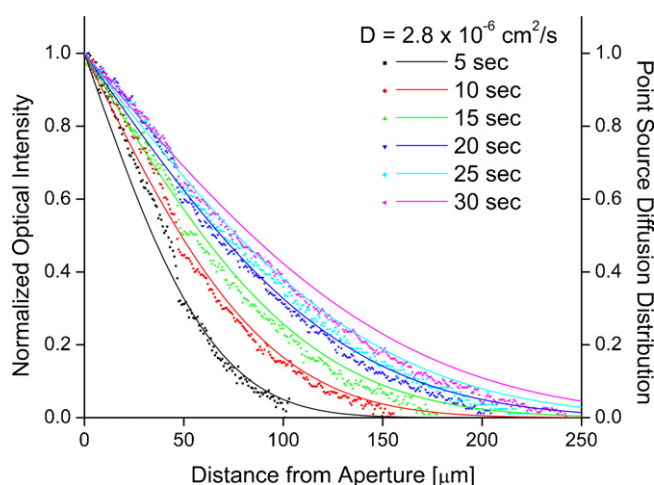


**Fig. 16.** Fluid delivery of Rhodamine B by diffusion (dots) into DI water compared to point source diffusion theory (solid lines) from a 10  $\mu\text{m}$  pore. Reprinted from Chang, L.Y. et al., Integrated Flow Sensing for Focal Biochemical Stimulation, NEMS 2008, © 2008 IEEE.



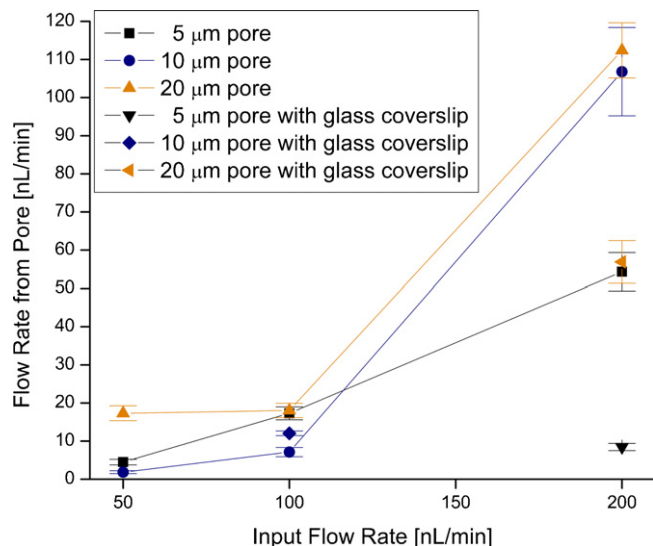


**Fig. 17.** Flow rates from different sized pores at different flows in the microchannel (mean  $\pm$  S.D. with  $n \geq 3$ ).

this model can then be used to predict and plan concentration profiles of released soluble factors. Experimentally, it was determined that the diffusion plume exhibited an average diffusion rate of  $4.9 \mu\text{m/s}$  from the  $10 \mu\text{m}$  pore (data not shown).

Data for fluid delivery by syringe pump-driven ejection with and without a flow limiting glass coverslip were obtained (Fig. 17). The influence of pore size on the flow rate is clearly observed at  $200 \text{ nL/min}$  but less obvious at lower flow rates when no glass coverslip is placed over the pore. The presence of the glass coverslip reduces the flow rate compared to the case without in all instances. Some evaporative fluid loss may occur without the coverslip, especially since the data is acquired under magnification in a compound optical microscope. The presence of the glass coverslip eliminates fluid loss but also limits fluid delivery. In future studies with cells cultured near the pore, both situations will be investigated. Cells

cultured directly on the device will mimic the first case in which there is no glass coverslip. Cells will also be culture on a coverslip and inverted over the pore to mimic the latter case with a glass coverslip.

#### 7.5. Tissue study with diffusion and ejection

Delivery of Rhodamine B from the pore to retinal tissue was demonstrated in two fluid delivery modes: diffusion and ejection. Time-lapse fluorescence microscopy images were captured in both modes showing dye accumulation over time in the tissue (Fig. 18). The rate of accumulation of dye within the tissue in ejection mode is visibly more pronounced than in diffusion mode. This is expected since diffusion is mass transport limited which effectively reduces the dye delivered to the tissue compared to ejection.

### 8. Conclusion

A microfluidic platform for precise focal delivery of soluble factors to cells and tissues was demonstrated. An array of three Parylene microchannels each centrally perforated with a uniquely sized small diameter pore were investigated. This arrangement allows a one-to-one correlation between the flow delivery channel and each pore. Each channel possesses Pt thermal flow sensors for integrated flow sensing. Focal fluid delivery capabilities of the system were characterized by calibration and operation of the thermal flow sensors, investigation of delivery in different modes through different sized pores, and preliminary demonstration of focal fluid delivery to tissue. The thermal flow sensors operated under steady state conditions were able to detect  $\text{nL/min}$  flow rates.

Future work entails feedback control of fluid flow with the flow sensors for precise delivery of soluble factors through the pore. Future work also includes culturing of cells on top of the microfluidic platform for in vitro studies of cells with precise  $\text{nL/min}$  flow rate focal delivery of soluble factors. High-density arrays of individually controlled pores will allow for more sophisticated interfaces to tissues and cells and greatly enhance the ability of researchers to address complex biological questions.

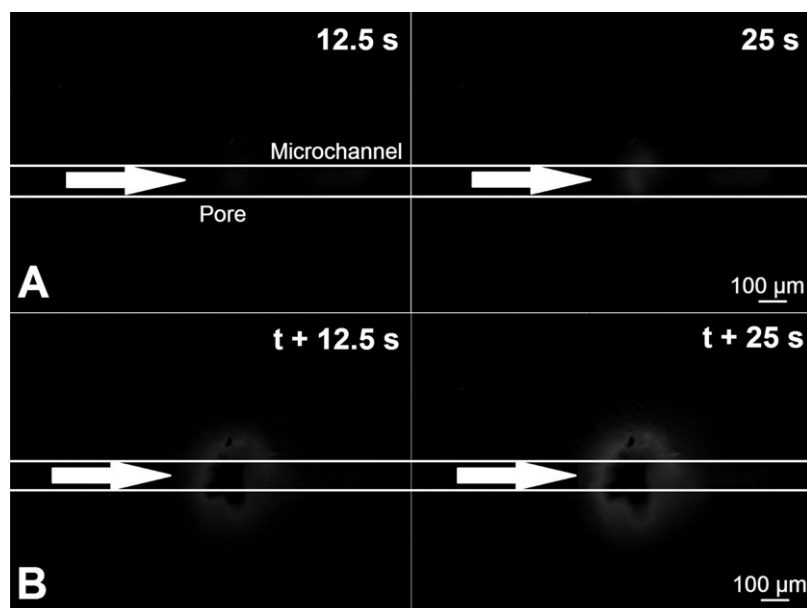


**Fig. 18.** (a) Fluorescence time-lapse images of focal delivery of Rhodamine B by diffusion to rat retina and (b) ejection mode time-lapse images focal delivery of Rhodamine B on the same tissue after diffusion. The arrow indicates the vicinity above the  $20 \mu\text{m}$  pore. The original image at time =  $0 \text{ s}$  was subtracted from the subsequent images after focal delivery start for both diffusion and ejection to highlight the difference in dye accumulation, hence the “donut” shape for the dye plume in (b).



## Acknowledgement

This work was funded in part by an NSF CAREER grant under Award Number EEC-0547544. The authors would like to thank Mr. Merrill Roragen and Dr. Donghai Zhu for fabrication assistance, Dr. David Merwine for providing the retinal tissue, and members of the Biomedical Microsystems Lab at the University of Southern California for their contributions to this work (especially Dr. Gabriela Mallén-Ornelas, Mr. Lingyun Zhao, Mr. Michael Wang, and Mr. Lawrence Yu).

## Appendix A. Supplementary data

Supplementary data associated with this article can be found, in the online version, at doi:10.1016/j.snb.2010.12.019.

## References

- [1] T.F. Kosar, A. Tourovskaia, X. Figueroa-Masot, M.E. Adams, A. Folch, A nanofabricated planar aperture as a mimic of the nerve-muscle contact during synaptogenesis, *Lab Chip* 6 (2006) 632–638.
- [2] A. Tourovskaia, T.F. Kosar, A. Folch, Local induction of acetylcholine receptor clustering in myotube cultures using microfluidic application of agrin, *Biophys. J.* 90 (2006) 2192–2198.
- [3] H.R. Bourne, O. Weiner, Cell polarity: a chemical compass, *Nature* 419 (2002) 21–21.
- [4] H. Lin, The stem-cell niche theory: lessons from flies, *Nat. Rev. Genet.* 3 (2002) 931–940.
- [5] H.J. Song, M.M. Poo, The cell biology of neuronal navigation, *Nat. Cell Biol.* 3 (2001) E81–E88.
- [6] A. Spradling, D. Drummond-Barbosa, T. Kai, Stem cells find their niche, *Nature* 414 (2001) 98–104.
- [7] D. Tosh, J.M.W. Slack, How cells change their phenotype? *Nat. Rev. Mol. Cell Biol.* 3 (2002) 187–194.
- [8] M. Ueda, Y. Sako, T. Tanaka, P. Devreotes, T. Yanagida, Single-molecule analysis of chemotactic signaling in dictyostelium cells, *Science* 294 (2001) 864–867.
- [9] M.C. Peterman, J. Noolandi, M.S. Blumenkranz, H.A. Fishman, Localized chemical release from an artificial synapse chip, *Proc. Natl. Acad. Sci. U.S.A.* 101 (2004) 9951–9954.
- [10] H. Kaji, M. Nishizawa, T. Matsue, Localized chemical stimulation to micropatterned cells using multiple laminar fluid flows, *Lab Chip* 3 (2003) 208–211.
- [11] S. Takayama, E. Ostuni, P. LeDuc, K. Naruse, D.E. Ingber, G.M. Whitesides, Selective chemical treatment of cellular microdomains using multiple laminar streams, *Chem. Biol.* 10 (2003) 123–130.
- [12] N.Z. Mehenti, H.A. Fishman, S.F. Bent, A model neural interface based on functional chemical stimulation, *Biomed. Microdev.* 9 (2007) 579–586.
- [13] J.T. Santini, M.J. Cima, R. Langer, A controlled-release microchip, *Nature* 397 (1999) 335–338.
- [14] B. Vastag, Future eye implants focus on neurotransmitters, *JAMA* 288 (2002) 1833–1834.
- [15] Q. Lin, F.K. Jiang, X.Q. Wang, Y. Xu, Z.G. Han, Y.C. Tai, J. Lew, C.M. Ho, Experiments and simulations of MEMS thermal sensors for wall shear-stress measurements in aerodynamic control applications, *J. Microelectromech. Syst.* 14 (2004) 1640–1649.
- [16] Q. Lin, Y. Xu, F.K. Jiang, Y.C. Tai, C.M. Ho, A parametrized three-dimensional model for MEMS thermal shear-stress sensors, *J. Microelectromech. Syst.* 14 (2005) 625–633.
- [17] E. Meng, P.Y. Li, Y.C. Tai, A biocompatible Parylene thermal flow sensing array, *Sens. Actuators A: Phys.* 144 (2008) 18–28.
- [18] E. Meng, Y.-C. Tai, A Parylene MEMS Flow Sensing Array, in: *Transducers 2003*, Boston, MA, 2003, pp. 686–689.
- [19] T.Q. Hoang, L.J. Ho, K. Swertfager, A. Gill, K. Malhotra, C. Jones, Surface Treatment Strategies for Microfluidic Devices Towards Longitudinal PC12 Neuronal Cell Studies, in: *Microtechnologies in Medicine and Biology*, Quebec City, Canada, 2009, pp. 212–213.
- [20] E. Meng, Y.-C. Tai, Parylene Etching Techniques for Microfluidics and BioMEMS, *MEMS 2005*, Miami, FL, 2005, 568–571.
- [21] E. Meng, P.J. Chen, D. Rodger, Y.C. Tai, M. Humayun, Implantable parylene MEMS for glaucoma therapy, *Eng. Med. Biol. Soc. Ann.* (2005) 116–119.
- [22] T.Y. Chang, V.G. Yadav, S. De Leo, A. Mohedas, B. Rajalingam, C.L. Chen, S. Selvarasah, M.R. Dokmeci, A. Khademhosseini, Cell and protein compatibility of parylene-C surfaces, *Langmuir* 23 (2007) 11718–11725.
- [23] Y.X. Kato, I. Saito, H. Takano, K. Mabuchi, T. Hoshino, Comparison of neuronal cell adhesiveness of materials in the diX (Parylene) family, *Neurosci. Lett.* 464 (2009) 26–28.
- [24] J.I. Kroschwitz, Kirk-Othmer Encyclopedia of Chemical Technology, John Wiley & Sons, Inc., New York, 1998.
- [25] J. Lahann, Vapor-based polymer coatings for potential biomedical applications, *Polym. Int.* 55 (2006) 1361–1370.
- [26] B.A. Weisenberg, D.L. Mooradian, Hemocompatibility of materials used in microelectromechanical systems: Platelet adhesion and morphology in vitro, *J. Biomed. Mater. Res.* 60 (2002) 283–291.
- [27] D. Dittmann, R. Ahrens, Z. Rummeler, K. Schlote-Holubek, W.K. Schomburg, Low-cost flow transducer fabricated with the AMANDA-process, in: *Transducers'01*, Munich, Germany, 2001, pp. 1472–1475.
- [28] J.W. Gardner, *Microsensors: Principles and Applications*, John Wiley & Sons, Inc., Chichester, New York, 1994.
- [29] K.G. Kreider, F. DiMeo, Platinum/palladium thin-film thermocouples for temperature measurements on silicon wafers, *Sens. Actuators A: Phys.* 69 (1998) 46–52.
- [30] F. Mailly, A. Giani, R. Bonnot, P. Temple-Boyer, F. Pascal-Delannoy, A. Foucaran, A. Boyer, Anemometer with hot platinum thin film, *Sens. Actuators A: Phys.* 94 (2001) 32–38.
- [31] J. van Honschoten, J. van Baar, H.E. de Bree, T. Lammerink, G. Krijnen, M. Elwenspoek, Application of a microflow as a low-cost level sensor, *J. Micromech. Microeng.* 10 (2000) 250–253.
- [32] K.M. Vaeth, K.F. Jensen, Transition metals for selective chemical vapor deposition of parylene-based polymers, *Chem. Mater.* 12 (2000) 1305–1313.
- [33] N.-T. Nguyen, Thermal mass flow sensors, in: J.G. Webster (Ed.), *The Measurement, Instrumentation, and Sensors Handbook*, CRC Press, Boca Raton, FL, 1999.
- [34] N.T. Nguyen, R. Kiehnscherf, Low-cost silicon sensors for mass flow measurements of liquids and gases, *Sens. Actuators A: Phys.* 49 (1995) 17–20.
- [35] S. Matsumoto, J. Xie, Y.C. Tai, Polymer micro interface for fluidic probing, in: *2003 Micro Total Analysis System (uTAS'03)*, Squaw Valley, CA, USA, 2003, pp. 551–554.
- [36] K. Chattopadhyay, S. Saffarian, E.L. Elson, C. Frieden, Measurement of microsecond dynamic motion in the intestinal fatty acid binding protein by using fluorescence correlation spectroscopy, in: *Proceedings of the National Academy of Sciences of the United States of America*, 99, 2002, pp. 14171–14176.

## Biographies

**Jonathan T.W. Kuo** received the B.S. degree in bioengineering from the University of California, San Diego, in 2007. He is currently working towards the Ph.D. degree in biomedical engineering at the University of Southern California, Los Angeles. His research interest lies in using bioMEMS to create biosensors.

**Li-Yuan Chang** received the B.S. degree in biomedical engineering from the University of California, San Diego, in 2003, and the M.S. degree in Medical Device and Diagnostic Engineering from the University of Southern California, Los Angeles, in 2007. Since 2008, he has joined Citibank Commercial Banking Division in Taiwan specializing in company valuations and loan originations for small medium enterprises in pharmaceutical and medical space.

**Po-Ying (Brian) Li** received the B.S. and M.S. degree in mechanical engineering from the Tatung Institute of Technology, Taipei, Taiwan, in 1996 and the National Tsing Hua University, Hsinchu, Taiwan, in 2001. He also received a M.S. degree in materials science in 2004 and a Ph.D. degree in electrical engineering in 2009 from the University of Southern California, Los Angeles. Currently, he is a Micro Device Engineer at the Replenish, Inc. He was a research assistant member with the National Science Foundation Biomimetic MicroElectronic Systems Engineering Research Center (BMES ERC) in the University of Southern California from 2004 to 2009. His research focused on the fabrication and characterization of the first implantable bioMEMS intraocular drug delivery device for the treatment of glaucoma and age-related macular degeneration. Dr. Li is a member of Eta Kappa Nu (HKN), Sigma Xi, Institute of Electrical and Electronics Engineers (IEEE), American Society of Mechanical Engineers (ASME), American Chemical Society (ACS), and American Vacuum Society (AVS).

**Tuan Hoang** received the B.S. degree in biological sciences from the California Institute of Technology, Pasadena in 1995. He was a graduate student in the Interdepartmental Ph.D. Program for Neuroscience at UCLA from 1997 to 2004. Since 2006, he is a faculty member in the Department of Biomedical Engineering, University of Southern California, Los Angeles. His research interest is to apply neuroengineering principles for the study of neurodegeneration and neurorepair. He was a recipient of the Caltech-Ahmanson Foundation scholarship from 1992 to 1995 and a NIH predoctoral training grant for molecular and cellular biology from 1999 to 2001. He was a member of the International Society of Magnetic Resonance in Medicine from 1996 to 1998 and a member of the Society of Neuroscience from 1998 to 2004.

**Ellis Meng** received the B.S. degree in engineering and applied science and the M.S. and Ph.D. degrees in electrical engineering from the California Institute of Technology (Caltech), Pasadena, in 1997, 1998, and 2003, respectively. She is an associate professor in the Department of Biomedical Engineering, University of Southern California, Los Angeles, where she has been since 2004. She currently holds a joint appointment in the Ming Hsieh Department of Electrical Engineering. Her research interests include bioMEMS, implantable biomedical microdevices, microfluidics,

multimodality integrated microsystems, and packaging. She was the Thrust Leader for Interface Technology and the Associate Director of Education and Student Diversity Researcher at the National Science Foundation's Biomimetic MicroElectronic Systems Engineering Research Center. She held the Viterbi Early Career Chair in the Viterbi School of Engineering. Dr. Meng is a member of Tau Beta Pi, the Biomedical Engineering Society, the Institute of Electrical and Electronics Engineers, the

American Society of Mechanical Engineers, the Society of Women Engineers, and the American Society for Engineering Education. She was a recipient of the Intel Women in Science and Engineering Scholarship, the Caltech Alumni Association Donald S. Clark Award, and the Caltech Special Institute Fellowship. She has also received the NSF CAREER and Wallace H. Coulter Foundation Early Career Translational Research Awards.